Surface spin canting in Fe_3O_4 and $CoFe_2O_4$ nanoparticles probed by high-resolution electron energy loss spectroscopy

D. S. Negi,[1,2] H. Sharona,[1,2] U. Bhat,[1,2] S. Palchoudhury,[4] A. Gupta,[3] and R. Datta[1,2,*]

[1]*International Centre for Materials Science, Jawaharlal Nehru Centre for Advanced Scientific Research, Bangalore 560064, India*

[2]*Chemistry and Physics of Materials Unit, Jawaharlal Nehru Centre for Advanced Scientific Research, Bangalore 560064, India*

[3]*Center for Materials for Information Technology, University of Alabama, Tuscaloosa, Alabama 35487, USA*

[4]*Civil and Chemical Engineering, University of Tennessee at Chattanooga, Chattanooga, Tennessee 37403, USA*

(Received 5 January 2017; revised manuscript received 28 April 2017; published 30 May 2017)

High-resolution electron energy loss spectroscopy (HR-EELS) is utilized to probe the surface spin canting in nanoparticles of two technologically important magnetic materials, i.e. Fe_3O_4 and $CoFe_2O_4$ (CFO). A soft experimental technique has been developed that is capable of extracting EELS spectra with single atomic plane resolution recorded in a single frame. The technique yields information at different depths of the nanoparticle from the surface to the core regions with high signal-to-noise ratio and without beam damage. This enables comparing the fine structures between the surface and core regions of the nanoparticles. The results confirm earlier observations of uniformly oriented spin canting structure for CFO and provide additional information regarding atom site-selective spin canting information. In the case of Fe_3O_4, preferred canting orientation forming core and shell structure is deduced. Unlike earlier reports based on polarized spin-flip neutron scattering measurement, it is possible from the experimental spectra combined with the first principle-based calculations considering noncollinear magnetism to narrow down the canting angles for Fe_3O_4 (T_d, O_h tilts 40°, 40°) and CFO (T_d, O_h tilts 17°, 17°). In addition, the role of Dzyaloshinskii-Moriya interaction in stabilizing the spin canting at the nanoparticle surface is discussed. The results demonstrate that HR-EELS can be a powerful technique to probe the magnetic structure in nanodimensional systems and has advantages over neutron-based techniques in terms of superior spatial resolution, site-specific information, and ease of sample preparation.

DOI: 10.1103/PhysRevB.95.174444

I. INTRODUCTION

Magnetic nanoparticles, particularly Fe_3O_4 and $CoFe_2O_4$ (CFO), have found a wide range of applications in areas such as biomedicine for hyperthermia-based cancer treatment, drug delivery, magnetic resonance imaging (MRI) contrast agents, bio-imaging, spintronics, high-density data storage, etc. [1–10]. The prerequisite for all these applications is large magnetic response even at nanometer dimension. However, it is often found that the saturation magnetization in nanoparticles is significantly reduced compared to their bulk counterpart [11–13]. Surface spin canting due to broken symmetry, surface spin disordering, crystallographic changes, and magnetic dead layers at the surface are generally considered to be responsible for the reduced saturation magnetization (M_s) with respect to their bulk counterpart. This significantly reduces the practical efficiency and sensitivity of such nanoparticles [14–18]. There is considerable interest in characterizing and understanding the surface spin structure of magnetic nanoparticles from the point of view of fundamental science as well as improvements in synthesis procedures [19–25]. Research is actively being pursued to understand the surface spin geometry for various nanodimensional systems, and several experimental techniques have been developed in the recent past to attain such information [26–37].

Among various techniques to probe the surface spin geometry, two-dimensional (2D) polarization analyzed small angle spin-flip neutron scattering (PASANS) has recently been developed to determine the three-dimensional spatial distribution of spin moments in a dense face centered cubic assembly of iron oxide (Fe_3O_4, size ∼9 nm) and CFO (size ∼11 nm) nanoparticles [38,39]. The method is based on first detecting a negative cross term in the neutron spin-flip scattered intensity [$I_{SF}(\vec{Q})$] and then fitting an energy balance model to estimate the possible sets of canting angles and shell thicknesses. A correlated phase factor $\overline{\cos}(\delta\varphi)$ between magnetic distributions parallel [$|M_{\parallel\vec{H}}(\vec{Q})|$] and perpendicular [$|M_{\perp\vec{H}}(\vec{Q})|$] to the applied field indicates the presence of core-shell geometry in the ensemble of nanoparticles. The analysis revealed magnetic core-shell morphology and a uniformly canted structure for Fe_3O_4 and CFO nanoparticles, respectively. The energy balance model is dominated by Zeeman energy vs exchange energy and Zeeman energy vs anisotropy energy for Fe_3O_4 and CFO nanoparticles, respectively. The analysis inferred a range of canting angles $\varepsilon = 27$ to 42° at 200 K and $\varepsilon = 23$ to 31° at 300 K with corresponding shell thickness of 1.0 ± 0.2 nm and 1.5 ± 0.2 nm for Fe_3O_4 at 1.2 T of magnetic field. At 10 K, canting angles ε in terms of T_d tilt in the range of 50 to 85° with a wide mix of shell thicknesses is obtained. At 300 K and 0.005 T remnant field, a preferred T_d tilt = 5° with no definite shell thickness is derived based on the energy balance model. For CFO, canting angles of 33 and 17° have been deduced at 10 and 300 K, respectively. The effect of temperature has been introduced in the energy balance model in terms of $m \propto \beta$, where β is the ratio of nanoparticle magnetization (m) to that of the bulk crystal (m_s). Though the technique certainly represents a powerful and pioneering development in understanding magnetic geometry at the nanoscale, it requires a large assembly of nanoparticles forming an ordered

*Corresponding author: ranjan@jncasr.ac.in

crystal lattice to obtain such information, where the presence of capping layer and interparticle dipolar interaction cannot be avoided. Moreover, it may often be difficult to form such an ordered crystal lattice of the nanoparticles with internal crystallographic symmetry aligned between them, which will likely lead to significant scatter in the recorded spin distributions. Moreover, smaller particle size may give rise to additional problems.

Alternative experimentation has been conducted in a transmission electron microscope (TEM) on individual magnetic nanoparticles based on electron energy loss spectroscopy (EELS) to obtain equivalent magnetic information with high spatial and energy resolution. Two different EELS-based techniques have been utilized so far to investigate the surface magnetism in nanoparticles: electron magnetic chiral dichroism (EMCD) and spatially resolved high-resolution EELS (HR-EELS) [26,40]. The principle of EELS is based on interpreting the signal in terms of density of unoccupied states, which is sensitive to any changes in the electronic structure in the material, and in the present case, it is the geometrical arrangement of spins. While EMCD revealed qualitative difference (∼30%) in magnetic order between the surface and interior of Fe_3O_4 nanoparticles [40], HR-EELS technique could quantify the difference in overall magnetic order between the regions with and without capping agents in the case of $CuCr_2S_4$ nanoparticles [26]. The HR-EELS-based technique indicated that capping agents help significantly restore the magnetic moment at the surface of the nanoparticles. Moreover, it helps to explain the large difference in m_s values between the spectroscopy and bulk magnetometry techniques in terms of unaccounted weight of the capping agents, which significantly underestimates the magnetization of nanoparticles by bulk magnetometry techniques [11,13,26].

In this paper, we have further extended the HR-EELS technique to probe the surface spin canting in Fe_3O_4 and CFO nanoparticles. The technique is based on experimentally recording the fine features in the HR-EELS spectra combined with the first principle-based calculations using WIEN-NCM code [41]. The code can simulate changes in electronic structure due to spin canting at various angular configurations with respect to the usual ferrimagnetic configuration. Additionally, we have considered the Dzyaloshinskii-Moriya (DM) interaction due to spin canting and ascertained that DM energy savings can also stabilize the spin canting geometry at the surface due to broken symmetry other than the Zeeman energy term, which otherwise requires application of an external field. However, the Zeeman term is important since it further helps to form a core-shell structure. To understand the surface spin structure and spatial distribution of magnetic response from a single nanoparticle, it is essential to distinguish the magnetic response from the core and surface regions separately. Therefore, the experimentation required development of a soft technique to obtain high-quality spectra capable of providing single atomic plane resolution without damaging the particles, along with all the information being recorded in a single exposure frame. The usual choice of scanning TEM-EELS (STEM-EELS) combination usually results in drilling holes in most nanoparticle samples, thus preventing the collection of spectra with sufficiently long exposure time [26,42]. The overall results of this paper are consistent with those from previous neutron-based experiments, suggesting that a core and canted shell are formed in the case of Fe_3O_4 and uniformly canted configuration occurs in the case of CFO. Additional information is obtained on atom site-selective spin canting. Moreover, the first principle-based method in combination with the experimentation has helped to narrow down the canting angle for Fe_3O_4 (T_d, O_h tilts 40°, 40°) and CFO (T_d, O_h tilts 17°, 17°) for the measurements carried out at 300 K. We infer different shell thicknesses at two different temperatures, i.e. 77 and 300 K for Fe_3O_4 and for CFO, respectively. The results indicate that HR-EELS can indeed be used to probe the fine details of spin structure at the nanoparticles surface, and the same can be extended to other nanodimensional magnetic systems.

II. EXPERIMENTAL AND THEORETICAL TECHNIQUES

Nanoparticles of Fe_3O_4 and CFO are prepared by thermolysis of Fe^{+3}-oleate and mixed $Co^{+2}Fe^{+3}$-oleate complex, respectively, following our previously published protocol [13,43]. In a typical synthesis of Fe_3O_4 nanoparticles, iron oleate (2 mmol) is thermally decomposed at 320 °C for 2.5 h in the presence of oleic acid (0.1 mL)/trioctylphosphine oxide (0.2 g) surfactant mixture in 1-octadecene under N_2 atmosphere. Similarly, mixed $Co^{2+}Fe^{3+}$-oleate precursor (2 mmol) is heated at 320 °C for 1 h under inert gas protection in the presence of capping agent, oleic acid (0.2 g) dissolved in 1-octadecene (6 mL), to form CFO nanoparticles.

High-resolution transmission electron microscopy (HR-TEM) and HR-EELS are performed in a double aberration correction transmission electron microscope, FEI Titan3, 80–300 kV equipped with a gun monochromator. All the spectra are collected with a Gatan imaging filter (GIF) entrance aperture of 1 mm and energy dispersion of 0.03 eV/channel. For achieving high spatial resolution, the obvious choice is to work with a STEM-EELS combination mode. However, for most of the crystals, the STEM probe drills holes in the area of interest [Figs. S1(a)–S1(c)] due to high beam current before a quality spectrum can be recorded. Therefore, we have developed a soft experimental technique based on EELS with monoprobe [Fig. 1(a)], where first the nanoparticle of interest is placed at the center of the GIF entrance aperture [Fig. 1(b)] with atomic resolution image and then collecting the spectra in Y vs ΔE, equivalent to q vs ΔE in the diffraction image [Fig. 1(c)]. The images and spectra have direct correlation in terms of spatial information and corresponding spectra when one of the two spatial dimensions is folded or projected at every point to another perpendicular axis. The spectra extracted from each slice [Fig. 1(c)] have information from the projected area of the nanoparticles as marked in the Fig. 1(b). Extracted spectra are shown in Figs. 1(d) and 1(e). With this method, it is possible to obtain spatial resolution of single atom plane; however, the narrowest slice width chosen is ∼1−2 nm, which is sufficient for this paper. The technique can be considered possessing features of both the energy filtered TEM (EF-TEM) and STEM-EELS technique. The spatial axis Y and energy dispersion axis ΔE are common to EF-TEM and STEM-EELS, respectively. In an aberration corrected microscope in combination with monochromator, the spatial resolution is expected to be limited by delocalization effect; however, this should not

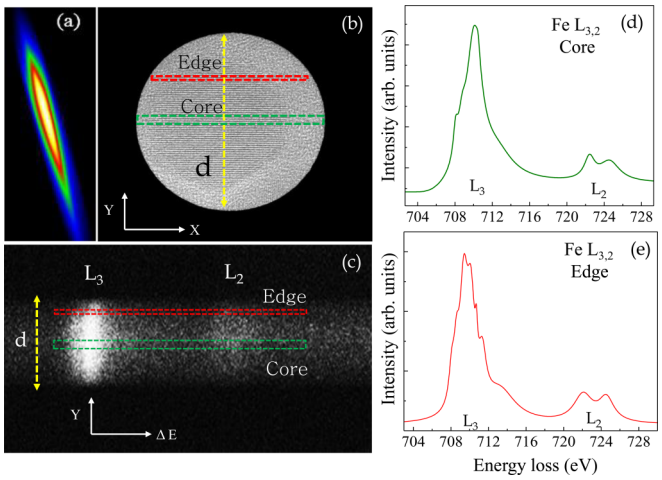

FIG. 1. Details of the soft HR-EELS-based technique with single atomic plane resolution. (a) Image of monoprobe that is used to illuminate the nanoparticle sample, (b) example atomic resolution image of ∼25 nm Fe_3O_4 nanoparticle as seen through 1 mm GIF entrance aperture in the image mode of spectrometer. In the spectroscopy mode, the entire image of (b) is dispersed as Y vs ΔE as shown in (c). Every Y data point in (c) has all the corresponding X data points projected in it. Rectangular slice tool is used to extract spatially resolved HR-EELS spectra from the (d) core and (e) edge of the nanoparticle with high signal-to-noise ratio.

prevent extracting EELS signal at atomic plane resolution (see Supplemental Material [37] and Refs. [44,45]). The added advantage of the technique is that it permits one to collect spectra in low dose parallel illumination mode and thus allows acquisition of spectra for sufficiently long exposure time without damaging the specimens along with monoprobe illumination, which is essential to preserve the high-energy resolution information. Moreover, all the spatial information is encoded in one single acquisition frame. Previously, a similar approach has been utilized, except for very high spatial resolution, where a probe area as small as ∼2 nm^2 is obtained by magnifying the specimen and using GIF as a selected area aperture, and any loss in signal due to magnification can be compensated by demagnifying the monoprobe on the sample, which acts as an independent control system in a microscope equipped with a gun monochromator [26]. The experiments have been performed at two different temperatures, namely 77 and 300 K. The described method can be extended to extract EMCD signal from a spatially resolved nanometer length scale area (see Figs. S2 and S3 in the Supplemental Material [37]). All the spectra have been acquired with a background magnetic field ∼2 T from the objective lens of the microscope.

We have carried out first principle-based calculations of total energy, cohesive energy, density of states (DOS), and EELS spectra for both Fe_3O_4 and CFO using WIEN2k code [46]. WIEN2k is a full potential linearized augmented plane wave + local orbitals (LAPW + LO) method within the framework of density functional theory (DFT). Various canting configurations of tetrahedral and octahedral tilts, i.e. T_d, O_h as well as relative tilts between them, such as both tilt along reference axis and azimuthal orientations, are considered for

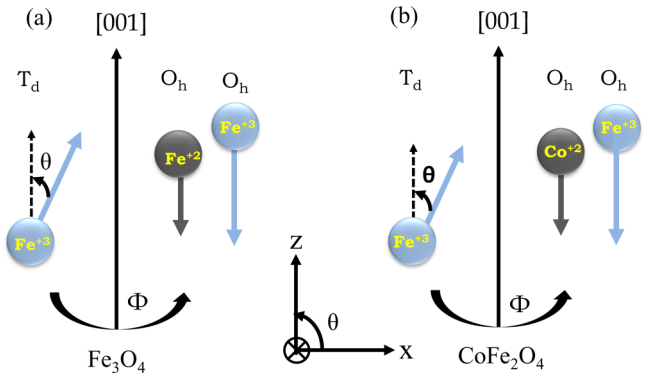

FIG. 2. Schematic representation of spin canting geometry for (a) Fe_3O_4 and (b) CFO nanoparticles with respect to the corresponding easy axis. Here, θ is the spin canting angle with respect to easy axis, and Φ is the azimuthal canting angle about easy axis. For example, only T_d canting is shown; however, any combination of canting in terms of θ, Φ is possible between the three different magnetic ions in the inverse spinel structure.

calculating relative stability over typical ferrimagnetic configurations using magnetic noncollinear WIEN-NCM code with atomic moment approximation (AMA) [41]. Figure 2 shows the reference axis for various tilt and azimuthal directions of spins with respect to the ferrimagnetic alignment. A schematic of various canted structures can be found in the Supplemental Material [37]. The lattice parameters are optimized with the Perdew-Burke-Ernzerhof (PBE) functional within the generalized gradient approximation (GGA). The RK_{max} value is set to 7.0. The criteria of convergence for force, energy, and electronic charge are set to below 1 mRy/au, 0.0001 Ry, and

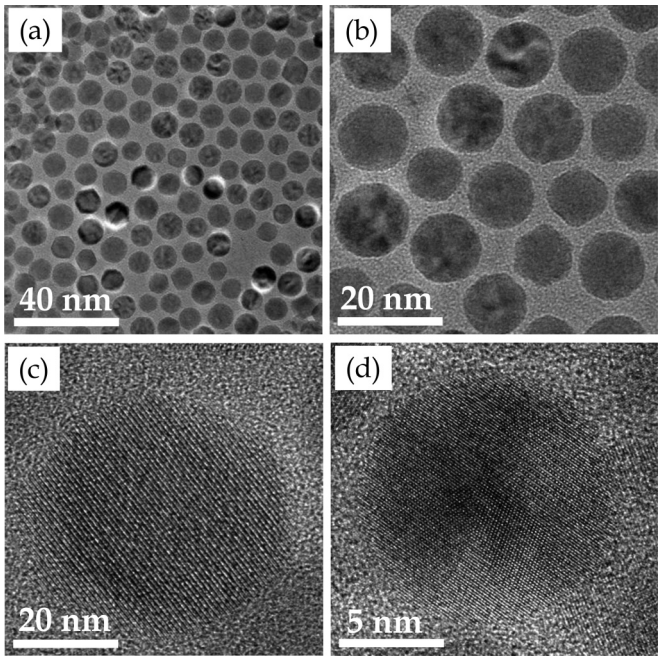

FIG. 3. (a) and (b) Low-magnification and (c) and (d) HR-TEM images of Fe_3O_4 and CFO nanoparticles, respectively. HR-TEM images show that the nanoparticles are single crystalline and free from any visible crystallographic defects.

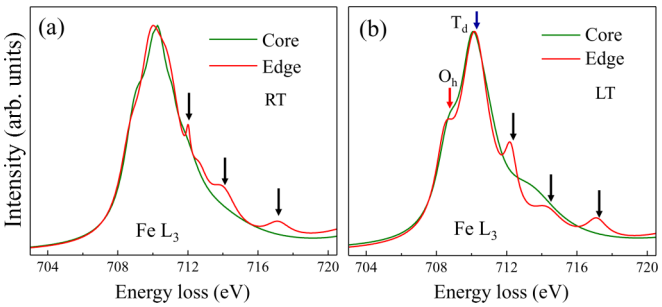

FIG. 4. Experimental L_3 spectra of Fe_3O_4 recorded (a) at room temperature and (b) at liquid nitrogen temperature (77 K). The spectra from the core and edge regions of the nanoparticles are colored with green and red, respectively. Dominating features from T_d and O_h atomic sites are marked. Fine features become more discrete in shape in the spectra taken from the edge region of nanoparticles.

0.001 e, respectively. The same optimized lattice parameters are used to calculate energy values corresponding to various spin canting arrangements. Further energy correction is done with GGA + U method, with U and J values taken from the Refs. [47,48]. The magnetic moments of Fe_3O_4 and CFO unit cell are 4 and 3 μ_B, respectively, and are consistent with the previous reports [49,50].

III. RESULTS AND DISCUSSION

Figures 3(a)–3(d) show the low magnification and HR-TEM images of well-dispersed nanoparticles of Fe_3O_4 and CFO, respectively. Most of the particles are single crystalline, and the crystallinity is preserved even at the surface. Particles with good crystallinity, i.e. without any visible crystallographic defects with representative shape and size are selected for this paper, as shown in the example individual particle image. The particles are capped with oleic acid for both Fe_3O_4 and CFO, which ensures dispersion and prevents agglomeration. The overall morphology of the particles is spherical with average diameters of 25 (±2) nm and 10 (±4) nm for Fe_3O_4 and CFO nanoparticles, respectively [13].

A. Fe_3O_4 nanoparticles

Figures 4(a) and 4(b) show representative experimental spectra for the Fe L_3 edge of a Fe_3O_4 nanoparticle from the core and interior regions at both 300 and 77 K. The spectra have been extracted by using a rectangular slice tool from the Y vs ΔE plot as described in the experimental section [Fig. 1(c)]. The slice width of the rectangular box is approximately 1–2 and 5–10 nm for the locations at the edge and center regions of the nanoparticles, respectively. This amplifies the relative spectral weights from the surface and bulk regions, respectively. Kindly see the discussion later in Sec. III B on how varying the rectangular slice width helps to estimate the approximate shell thickness of the nanoparticles. We have considered features only in the L_3 absorption edge and the complete spectra, i.e. $L_{3,2}$, are given in Figs. 1(d) and 1(e). The most significant tetrahedral and octahedral DOS contributions to the overall spectra are marked with arrows. The blue and red colored arrows indicate the tetrahedral and octahedral site contributions to the spectra, respectively. This has been done with the help of theoretically simulated spectra [Fig. 5(a)]. The changes in features due to surface spin canting are marked in the spectra with black arrows. To understand the changes in the features due to spin canting geometry, it is important to compare the results with the unoccupied DOS calculated by first principle method, which serves as a fingerprint in the absence of a standard experimental spectra with known spin canting configurations. As already mentioned, the EELS spectra contain information on the density of unoccupied states and are expected to be sensitive to the changes in electronic structure of the materials due to various spin canting arrangements. The changes are small and need careful analysis to discern the effect [44].

Figure 5(a) shows the simulated theoretical contributions from the tetrahedral and octahedral Fe to the overall EELS spectra. The partial d orbital contributions for the respective tetrahedral and octahedral atoms are shown in Figs. 5(b) and 5(c). The evolution of DOS has been studied systematically with different canting configurations. Various canting geometries have been considered, and the relative energy difference between them is provided in the Supplemental Material [37]. From the set of canting configurations considered for the calculation, the most stable configuration is T_d, O_h tilt of 40°, 40°, and the least stable is 20°, 0° (see Table S1(a) and S1(b) in the Supplemental Material [37]). Various azimuthal angles of spin orientations have also been considered for the most stable configurations and found not to change the stability of the system significantly (of the order of ∼0.02 meV); see Table S1(b) in the Supplemental Material [37]. The most stable

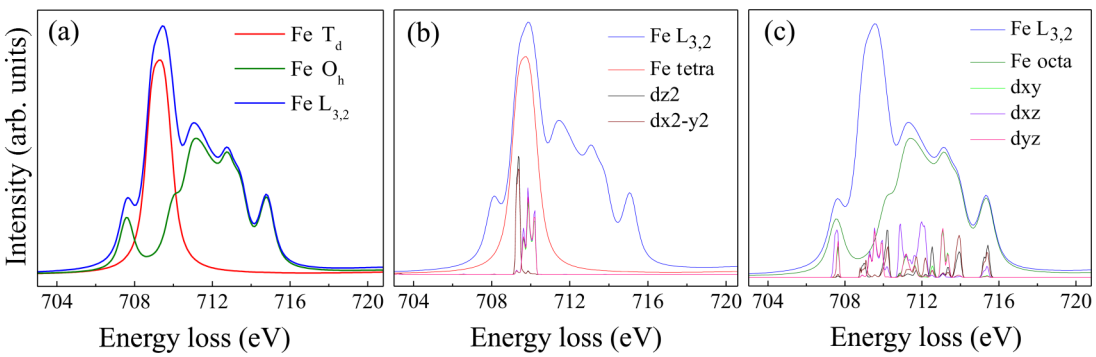

FIG. 5. Simulated Fe $L_{3,2}$ spectra in Fe_3O_4 shown with blue color. (a) T_d and O_h atomic contribution, (b) T_d contribution along with partial DOS, and (c) O_h contribution along with partial DOS to the averaged spectra are depicted with the aid of various color plots.

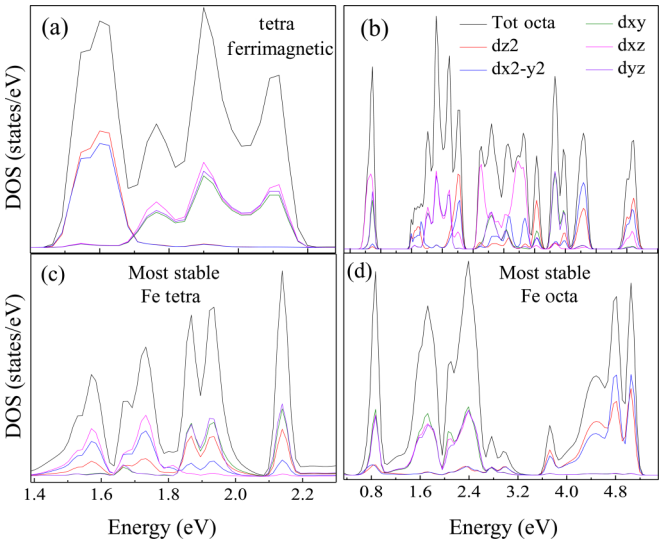

FIG. 6. Total density of unoccupied states (black line) with partial contributions for (a) T_d and (b) O_h Fe atoms in Fe_3O_4 with ferrimagnetic spin arrangement as calculated in WIEN-NCM code. The corresponding total DOS and partial contribution for most stable configuration for T_d and O_h atoms are given in (c) and (d), respectively.

canting configuration obtained from the present theoretical calculation falls in the higher end of the tilt range determined previously [38]. However, depending on the Zeeman energy term and competing energy, i.e. exchange energy, in the case of Fe_3O_4, the canting angle with higher net magnetic moment for the shell might be preferred, but the difference in magnetic moment between comparable canting geometries is not sufficiently different so that Zeeman energy contribution under a high enough magnetic field can supersede the overall penalty energy term of the system and thus assume the canting configurations with the higher magnetic moment. The density of unoccupied DOS for comparable canting configurations, including the most stable T_d, O_h tilt of 40°, 40° with respect to ferrimagnetic configuration, is shown in Fig. 6 for both tetra- and octahedral atomic sites. The primary difference between the ferrimagnetic and the canting cases is a decrease in bandwidth of neighboring DOS along with an increase in the energy gap between the DOS peaks with more discrete nature in the case of tetrahedral sites. For octahedral atomic sites, readjustment in the energy position of DOS and an increase in gap between the lower- to the higher-energy DOS can be noticed. However, it is difficult to distinguish features between the various types of canting configurations, except for slight differences in relative peak heights, and this requires careful correlation-based analysis and can be a topic of a future paper. Therefore, for this paper, because of the use of HR-EELS to probe canting geometry, we have limited ourselves to consider only the changes in the separation of peaks and their discrete nature to identify the occurrence of canting at the surface of the nanoparticles and roughly estimate the canting shell thickness. Therefore, the difference in the DOS between uncanted and canted states can be understood in terms of relative changes in the orbital overlap, thus leading to changes in terms of the discrete nature and relative spacing between the DOS peaks.

For the spectra recorded at 77 K, additional peaks are observed which are marked in Fig. 4(b). Overall, this is like the spectra at 300 K, except there are more peaks. These additional peaks are due to the monoclinic structure of Fe_3O_4 (space group 9 Cc) and is a result of the well-known Verwey transition at temperatures below 120 K in this system. The calculation for this monoclinic structure also shows the presence of peaks, which are different in number and positions in energy scale, contributing to the overall spectra (see Fig. S7 in the Supplemental Material [37]). Though the discrete nature from the surface areas indicates presence of canting, it will be worth performing first principle calculation for various spin canting configurations for such a monoclinic structure to determine the optimum spin canting angle in comparison to the inverse spinel structure. A similar difference in spectra at the two different temperatures is not observed in the case of CFO (see Sec. III B), demonstrating that HR-EELS is capable of detecting signatures due to such changes in the structural symmetry.

The primary difference between the energy balance model used in past reports and the present first principle-based calculation is that, for the former, analysis of the various energy costs associated with canting have been evaluated from the component of canted spin moment magnitude through the $[1 - \cos(\varepsilon)]$ dependence term, where ε is the canting angle at either the T_d or O_h site, whereas the first principle methods are quantum mechanical calculations and consider relative exchange and anisotropy energy costs for various noncollinear spin canting orientations with respect to other collinear spins in the crystal lattice. In fact, spin canting may increase or decrease the net magnetic moment in the unit cell (see Table S1 in the Supplemental Material [37]) that contributes to the Zeeman energy savings or penalty under an applied magnetic field that balances the dominant exchange energy and anisotropy energy penalty in the case of Fe_3O_4 and CFO, respectively. Spin canting is also associated with a noncollinear relationship in terms of spin arrangement with respect to collinear spins and will have additional DM interaction term in the general form

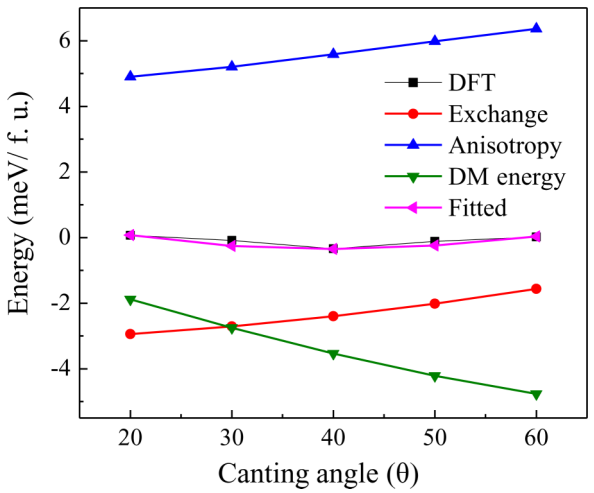

FIG. 7. Plot of the spin-dependent penalty energy cost calculated by DFT as a function of T_d canting angle for Fe_3O_4. The penalty energy cost is split into three competing energy terms: isotropic exchange energy (red line), anisotropy energy (blue line), and DM interaction energy (green line).

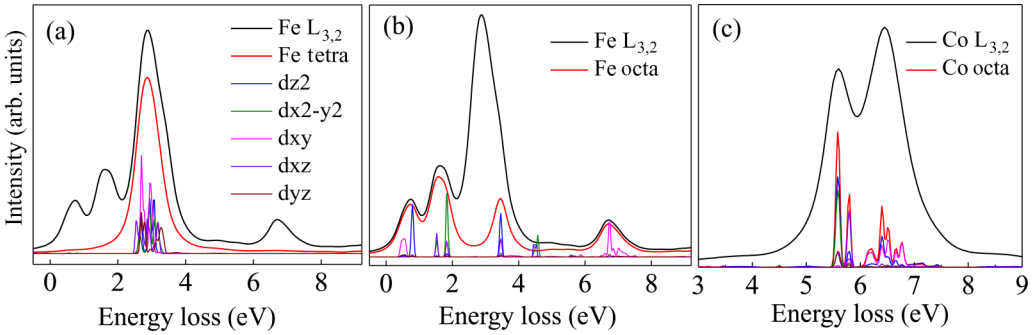

FIG. 8. Simulated Fe L_3 spectra in CFO shown with blue color. (a) T_d contribution along with partial DOS, and (b) O_h contribution along with partial DOS to the averaged spectra are depicted with the help of various color plots. (c) Co L_3 spectra with partial contributions of Co O_h DOS.

of bilinear coupling energy between two spins [51,52]. This noncollinear relationship between spin vectors in the crystal is responsible for the existence of the DM term in the case of Sr_2IrO_4, but cancellation in case of Ba_2IrO_4 [53,54]. However, the DM interaction has thus far not been considered in the context of surface spin canting of magnetic nanoparticles. The anisotropic exchange energy due to the DM interaction can also contribute to the stability of the canted spin configurations at the nanoparticle surface due to reduced symmetry in addition to the Zeeman energy term, which only appears in the presence of an external magnetic field. Therefore, additionally, we have explored in this paper the extent to which the DM term plays a role in stabilizing spin canting at the nanoparticle surface and balancing the dominant counterenergy term. The DM interaction is generally used to explain the observed weak ferromagnetism in antiferromagnetic materials where the interaction strength is either a few percent of or equivalent to the isotropic energy term [55]. Recently, methods have been developed to study the anisotropic magnetic coupling related to the DM coupling parameter. The method is based on first mapping magnetically constrained noncollinear DFT onto a general spin Hamiltonian [53,56–59], then by fitting the spin-related penalty contributions to the total energy, relative contributions, and balance between Heisenberg exchange, the DM interaction and the single ion anisotropy terms can be evaluated. The penalty energy can be written for the spin constrained calculation as [54]

$$\Delta E = E - E_0 = \sum_i \gamma \left[M_i - M_i^0 (M_i . M_i^0)\right]^2, \qquad (1)$$

where E_0 is the DFT energy and ΔE is the penalty energy due to noncollinear directional constraint. Here, M_i^0 is a unit vector along the global direction of the magnetic moment at site i, M_i is the integrated magnetic moment inside the Wigner-Seitz cell around atom i, and γ is the parameter through which the penalty energy term is controlled.

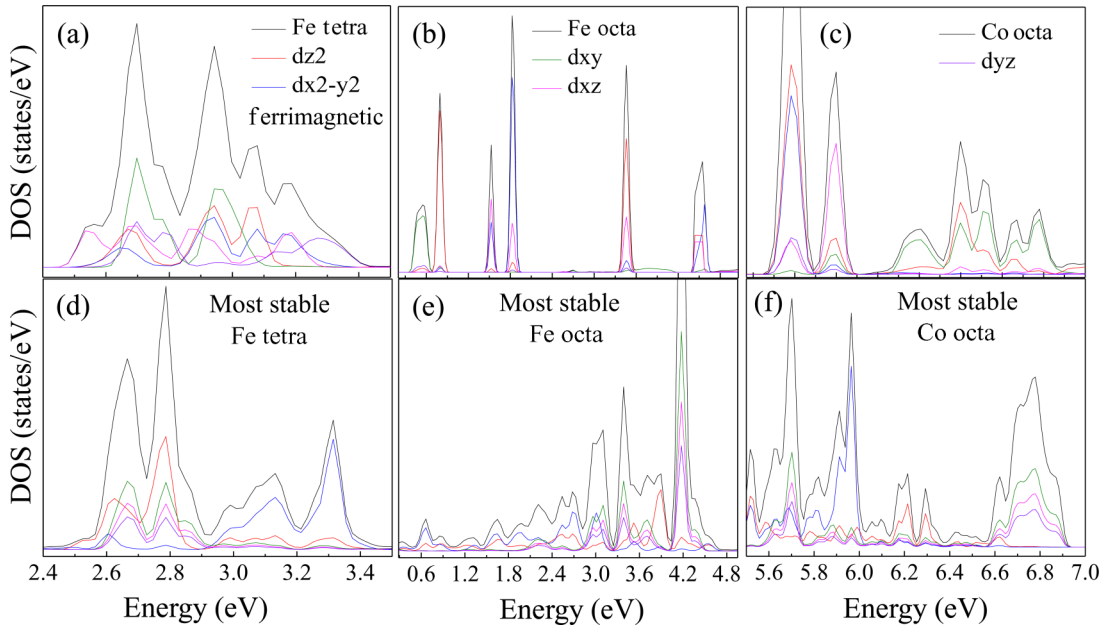

FIG. 9. Total density of unoccupied states (black line) with partial contributions for (a) O_h Co, (b) O_h Fe, and (c) T_d Fe in CFO with ferrimagnetic spin arrangement as calculated in WIEN NCM code. The corresponding total DOS and partial contribution for most stable configuration corresponding to (a), (b), and (c) are given in (d), (e), and (f), respectively.

By varying the spin canting angle, we obtain DFT+ spin-orbit coupling (SOC) + U total energy plot as shown in Fig. 7. Two different plots are shown: the first one is with varying canting angle of the T_d site, and the second one with varying azimuthal angle for the most stable T_d canting angle (40°). However, we have fitted the competing energy terms only for the first case, as energy difference between different azimuthal angles is an order of magnitude smaller. The penalty energy is then mapped onto the standard expression of the classical spin Hamiltonian [54]

$$\Delta E = -\sum_{i<j} J_{ij} S_i . S_j + \sum_i \varepsilon^i_{\text{an}}(S_i) + \sum_{i<j} D_{ij} . [S_i \times S_j]. \quad (2)$$

Here, the first, second, and third terms represent the isotropic Heisenberg exchange, the single ion anisotropy, and DM interaction. The above equation for ferrimagnetic Fe_3O_4 and CFO reduces to

$$\Delta E = 16 J S^2 \cos(\theta) + K[5 - \cos(2\theta)] - 16 D_z S^2 \sin(\theta), \quad (3)$$

and appears to be same for both the systems (see Supplemental Material [37]).

In the above equations J, K, and D_z are the isotropic exchange, single spin anisotropy, and DM exchange parameter, respectively. The procedure for deriving the above two expressions is given in the Supplemental Material [37].

Figures 7 and 11 plot the DFT penalty energy as a function of tetrahedral site canting for Fe_3O_4 and CFO, respectively. The fitting shows that the DM term balances the energy cost associated with isotropic exchange and the anisotropy term due to spin canting. The magnetic coupling parameters J, K, and D_z for Fe_3O_4 and CFO are given in Table S3 in the Supplemental Material [37]. The typical Zeeman energy term for a magnetic moment of $5\mu_B$ and applied field of 2 T is ~0.6 meV. The DM term has similar value in comparison to the Zeeman energy for Fe_3O_4, but is much lower in the case of CFO nanoparticles. However, the DM energy term extracted from the fitting exercise has uncertainty, and there may exist different possible values from such a fitting procedure, and it can be much lower compared to the Zeeman term in the case of Fe_3O_4. The extracted values do not match well with the bulk reference values of the respective materials. Thus, though DM can play a role in stabilizing a canted spin structure at the surface due to broken symmetry in the absence of applied magnetic field, the effect of the Zeeman term can be visualized as further propagation of canted regions inside the nanoparticles which is balanced by the competing energy terms, i.e. isotropic exchange and anisotropic energy, and define the shell thickness as discussed earlier [38]. Note that the DM term will not lead to the formation of core-shell structure. The consideration of the DM term in the present case is based on experimental evidence of spin-flip polarized neutron diffraction that spin canting structure exists in the present two systems, and this is suggestive of nonzero DM terms (see Supplemental Material [37]). The above analysis is carried out by considering various spin canting configurations in the bulk crystal, and the fitting values may be different for not considering true surface effects. This may not change the most stable canting configurations. The spin canting structures (but not the core-shell structure) in the present two systems likely form due to the finite size of the particles, like the existence of the DM term in some magnetic materials due to symmetry breaking [60].

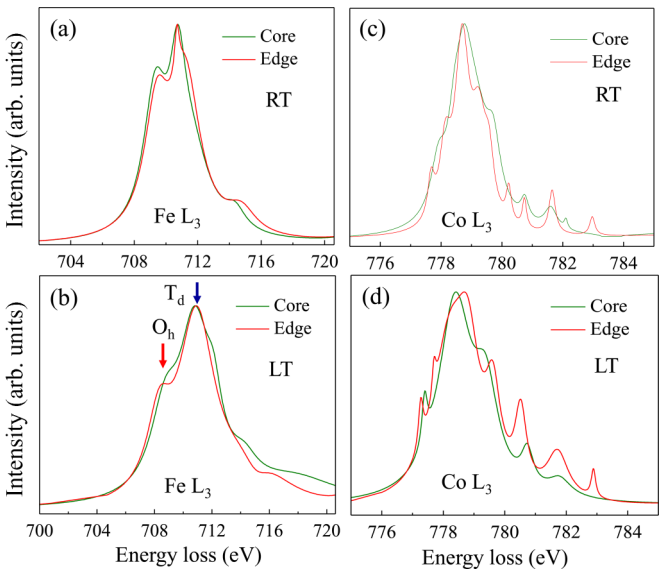

FIG. 10. Experimental L_3 spectra of CFO recorded (a) and (c) at room temperature and (b) and (d) at liquid nitrogen temperature (77 K) for Fe and Co atoms, respectively. The spectra from core and edge of nanoparticles are colored with green and red, respectively. Dominating features from T_d and O_h atomic sites are marked. Kindly note the fine features are only sharper for Co atoms, but not for Fe atoms, suggesting possible formation of uniformly oriented spin canting configuration for Fe atoms but core-shell morphology for Co atoms.

B. CFO nanoparticles

In contrast to Fe_3O_4, the WIEN-NCM calculation for CFO shows a smaller difference in cohesive energy or penalty energy between different canting configurations, which is of the order of ~0.001 eV compared to 0.01 eV in the case

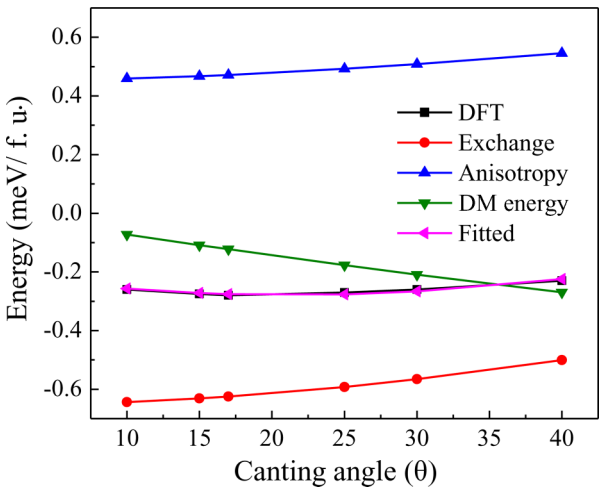

FIG. 11. Plot of the spin-dependent penalty energy cost calculated by DFT as a function of T_d canting angle for CFO. The penalty energy cost is split into three competing energy terms: isotropic exchange energy (red line), anisotropy energy (blue line), and DM interaction energy (green line).

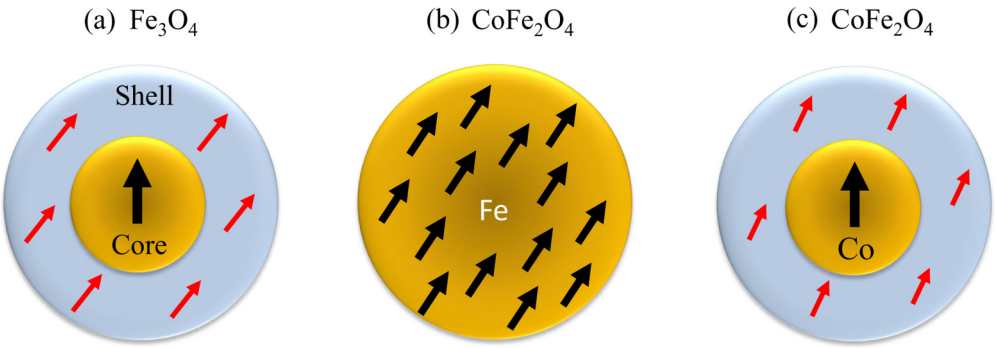

FIG. 12. Schematic of general spin canting geometry for (a) Fe_3O_4 and (b) and (c) for CFO nanoparticles. In the case of CFO, the Co atom forms the core shell canting configuration, but Fe forms the uniformly oriented canting configuration.

of Fe_3O_4. This indicates that, in CFO, the surface spins have the freedom to tilt along all possible directions (see Fig. S5 and Table S2 in the Supplemental Material [37]). The various canting configuration and their relative energies are given in Table S2(a) in the Supplemental Material [37]. The most stable configuration is 17° (both T_d and O_h), and the corresponding moment per unit cell volume is 4.12 μ_B. This specific configuration has two advantages, i.e. both the total energy and Zeeman energy savings due to maximum magnetic moment per formula unit under a magnetic field over other combinations. This is in close agreement with the earlier PASANS method where a canting angles of 17 and 33° have been predicted with the help of the energy balance model at 300 and 77 K, respectively [39]. Kindly note that, in the absence of a magnetic field, the DM term may stabilize canting structures with T_d 17°, O_h 17° having the most stable configuration. However, the exact canting angle due to DM contribution is not evident given the uncertainty in the fitting parameters.

Theoretical EELS spectra along with DOS for the usual ferrimagnetic spin configurations are shown in Fig. 8. The fine features corresponding to the Fe tetrahedral and octahedral atomic site contributions in the Fe L_3 spectra are marked with different colors. As Co is only in the octahedral site, therefore the fine features in the Co L_3 spectra will have contributions only from Co O_h DOS. Figure 9 shows how the distributions of DOS and discrete nature of peaks changes between the usual ferrimagnetic and the most stable (17°) spin canting configurations. For other canting configurations, see the Supplemental Material [37]. The theoretical changes are like the Fe_3O_4 case, and a quick distinction can be made only between the canted vs ferrimagnetic configurations, but a comparison between various canting configurations is not a simple task to perform and can be the prospect of a future paper.

Experimental Fe L_3 and Co L_3 spectra from two different regions of nanoparticles and at two different temperatures are shown in Fig. 10. The contributions from both tetrahedral and octahedral sites in the case of Fe and octahedral sites in the case of Co are indicated with arrows. Here, CFO does not undergo any structural transitions at low temperature, unlike the Fe_3O_4 case; therefore, a single structural model is sufficient to describe all the experimental spectra. Differences in peaks can only be observed between the core and edge regions of the CFO nanoparticles for Co L_3, but not for Fe L_3 spectra [Fig. 10]. The features in Fe L_3 suggest uniform canting of Fe spins throughout the nanoparticles, but a core-shell morphology for Co spins. This is a very important finding and demonstrates the capability of the HR-EELS technique in identifying atom-specific spin configurations, which may not be possible by neutron-based techniques. The theoretical calculations also suggest the formation of such a configuration due to the small energy difference compared to other spin canting geometry. From the experimental results, we find essentially similar features in terms of fine structures between the core and surface regions of the nanoparticles. Therefore, the EELS-based investigation agrees with earlier findings of a randomly oriented spin canting structure in the case of CFO based on experimental PASANS and an analysis based on an energy based model [39]. A value close to 17° is found to be the stable configuration at 300 K.

The shell thickness is determined approximately by sliding the rectangular slice with various widths below 1 nm and observing for discernable changes in the spectra. The changes in the spectra are between the corelike and edgelike features. This gives us approximately a shell thickness of 2 (±0.2) and 1.2 (±0.2) nm nm for Fe_3O_4 at 300 and 77 K, respectively, and 1.8 (±0.2) nm for the Co atom-only shell thickness for CFO. Figure 12 provides a schematic of the spin canting geometry for the two different nanoparticles.

IV. CONCLUSIONS

In conclusion, we have developed a soft experimental technique based on HR-EELS to probe the magnetic structure in magnetic nanoparticles with high spatial and energy resolution. The technique enables recording HR-EELS spectra with high signal-to-noise ratio without causing damage to the specimen. The technique has been utilized to investigate surface spin canting in both Fe_3O_4 and $CoFe_2O_4$ nanoparticles. The overall results are in good agreement with the previously reported polarized neutron-based technique, but the first principle calculations have helped us to narrow down the possible canting angles for Fe_3O_4 (T_d, O_h tilts 40°, 40°) and CFO (T_d, O_h tilts 17°, 17°). The possible role of DM interaction is also discussed and found to stabilize the spin canting structure at the surface, while the Zeeman energy term aids in forming the canted shell thickness upon balancing with the competing energy terms. These results represent an extension of the HR-EELS technique to probe magnetic spin canting in low-dimensional systems and can be further expanded to

address various other problems at the nanometer and atomic plane resolution length scale.

ACKNOWLEDGMENTS

The authors at International Centre for Materials Science (ICMS), Jawaharlal Nehru Centre for Advanced Scientific Research (JNCASR) sincerely thank Prof. C. N. R. Rao for his constant support and providing the advanced electron microscopy facility for this research. D.S.N. acknowledges CSIR India for a Ph.D. fellowship. The work at the University of Alabama was supported by the National Science Foundation under Grant No. CHE-1508259.

[1] C. C. Berry and A. S. G. Curtis, J. Phys. D: Appl. Phys. **36**, R198 (2003).
[2] K. E. Scarberry, E. B. Dickerson, J. F. McDonald, and Z. J. Zhang, J. Am. Chem. Soc. **130**, 10258 (2008).
[3] J. H. Lee, J. T. Jang, J. S. Choi, S. H. Moon, S. H. Noh, J. W. Kim, J. G. K. Kim, S. Kim, K. I. Park, and J. Cheon, Nat. Nanotech. **6**, 418 (2011).
[4] J. Xie, K. Chen, and X. Chen, Nano Res. **2**, 261 (2009).
[5] D. Bader, Rev. Mod. Phys. **78**, 1 (2006).
[6] N. Bao and A. Gupta, in *Encyclopedia of Inorganic and Bioinorganic Chemistry*, edited by R. A. Scott (John Wiley, Chichester, 2013).
[7] T. Hyeon, Chem. Comm. **8**, 927 (2003).
[8] F. Li, D. Zhi, Y. Luo, J. Zhang, X. Nan, Y. Zhang, W. Zhou, B. Qiu, L. Wen, and G. Liang, Nanoscale **8**, 2826 (2016).
[9] Q. A. Pankhurst, J. Connolly, S. K. Jones, and J. Dobson, J. Phys. D: Appl. Phys. **36**, R167 (2003).
[10] S. Sun, H. Zeng, D. B. Robinson, S. Raoux, P. M. Rice, S. X. Wang, and L. Guanxiong, J. Am. Chem. Soc. **126**, 273 (2004).
[11] K. Ramasamy, D. Mazumdar, Z. Zhou, Y. Hsiang, A. Wang, and A. Gupta, J. Am. Chem. Soc. **133**, 20716 (2011).
[12] Y. P. Cai, K. Chesnel, M. Trevino, A. Westover, R. G. Harrison, J. M. Hancock, S. Turley, A. Scherz, A. Reid, B. Wu, C. Graves, T. Wang, T. Liu, and H. Dürr, J. Appl. Phys. **115**, 17B537 (2014).
[13] N. Bao, L. Shen, Y. Wang, P. Padhan, and A. Gupta, J. Am. Chem. Soc. **129**, 12374 (2007).
[14] S. Linderoth, P. V. Hendriksen, F. Bardker, S. Wells, K. Davies, S. W. Charles, and S. Moup, J. Appl. Phys. **75**, 6583 (1994).
[15] M. P. Morales, C. J. Sernaz, F. Bødkerx, and S Mørupx, J. Phys.: Condens. Matter **9**, 5461 (1997).
[16] F. T. Parker, M. W. Foster, D. T. Margulies, and A. E. Berkowitz, Phys. Rev. B **47**, 7885 (1993).
[17] S. Kubickova, D. Niznansky, M. P. Morales Herrero, G. Salas, and J. Vejpravova, Appl. Phys. Lett. **104**, 223105 (2014).
[18] J. M. D. Coey, Phys. Rev. Lett. **27**, 17 (1971).
[19] S. Laurent, D. Forge, M. Port, A. Roch, C. Robic, L. V. Elst, and R. N. Muller, Chem. Rev. **108**, 2064 (2008).
[20] A. Lu, E. L. Salabas, and F. Schuth, Angew. Chem. Int. Ed. **46**, 1222 (2007).
[21] H. Deng, X. Li, Q. Peng, X. Wang, J. Chen, and Y. Li, Angew. Chem. **117**, 2842 (2005).
[22] N. A. Frey, S. Peng, K. Cheng, and S. Sun, Chem. Soc. Rev. **38**, 2532 (2009).
[23] D. L. Huber, Small **1**, 482 (2005).
[24] A. G. Kolhatkar, A. C. Jamison, D. Litvinov, R. C. Willson, and T. R. Lee, Int. J. Mol. Sci. **14**, 15977 (2013).
[25] J. Park, K. An, Y. Hwang, J. G. Park, H. J. Noh, J. Y. Kim, J. H. Park, N. M. Hwang, and T. Hyeon, Nat. Mater. **3**, 891 (2004).
[26] D. S. Negi, B. Loukya, K. Ramasamy, A. Gupta, and R. Datta, Appl. Phys. Lett. **106**, 182402 (2015).
[27] J. Verbeeck, P. Schattschneider, S. Lazar, M. Stoger-Pollach, S. Loffler, A. Steiger-Thirsfeld, and G. Van Tendeloo, Appl. Phys. Lett. **99**, 203109 (2011).
[28] F. Gazeau1, F. Boue, E. Dubois, and R. Perzynski, J. Phys.: Condens. Matter **15**, S1305 (2003).
[29] P. Schattschneider, I. Ennen, S. Löffler, M. Stöger-Pollach, and J. Verbeeck, J. Appl. Phys. **107**, 09D311 (2010).
[30] B. Loukya, X. Zhang, A. Gupta, and R. Datta, J. Magn. Magn. Mater. **324**, 3754 (2012).
[31] B. Loukya, D. S. Negi, K. Dileep, N. Pachauri, A. Gupta, and R. Datta, Phys. Rev. B **91**, 134412 (2015).
[32] E. O. Wollan and W. C. Koehler, Phys. Rev. **100**, 545 (1995).
[33] J. Verbeeck, H. Tian, and P. Schattschneider, Nature **467**, 301 (2010).
[34] A. Wiedenmann, Phys. B **356**, 246 (2005).
[35] S. Disch, E. Wetterskog, R. P. Hermann, A. Wiedenmann, U. Vainio, G. Salazar-Alvarez, L. Bergstrom, and T. Bruckel, New J. Phys. **14**, 013025 (2012).
[36] V. E. Dmitrienko, E. N. Ovchinnikova, S. P. Collins, G. Nisbet, G. Beutier, Y. O. Kvashnin, V. V. Mazurenko, A. I. Lichtenstein, and M. I. Katsnelson, Nat. Phys. **10**, 202 (2014).
[37] See Supplemental Material at http://link.aps.org/supplemental/10.1103/PhysRevB.95.174444 for the detail of particle damage by monoprobe, STEM probe, HR-EELS technique, various canting configuration considered for first principle calculation, DOS, and derivation of spin Hamiltonian for penalty energy with fitted exchange and anisotropy parameter.
[38] K. L. Krycka, J. A. Borchers, R. A. Booth, Y. Ijiri, K. Hasz, J. J. Rhyne, and S. A. Majetich, Phys. Rev. Lett. **113**, 147203 (2014).
[39] K. Hasz, Y. Ijiri, K. L. Krycka, J. A. Borchers, R. A. Booth, S. Oberdick, and S. A. Majetich, Phys. Rev. B **90**, 180405(R) (2014).
[40] J. Salafranca, J. Gazquez, N. Pérez, A. Labarta, S. T. Pantelides, S. J. Pennycook, X. Batlle, and M. Varela, Nano Lett. **12**, 2499 (2012).
[41] R. Laskowski, G. K. H. Madsen, P. Blaha, and K. Schwarz, Phys. Rev. B **69**, 140408 (2004).
[42] A. Garcia, A. M. Raya, M. M. Mariscal, R. Esparza, M. Herrera, S. Molina, G. Scavello, P. Galindo, M. J. Yacaman, and A. Ponce, Ultramicroscopy **146**, 33 (2014).
[43] N. Bao, L. Shen, W. An, P. Padhan, C. H. Turner, and A. Gupta, Chem. Mater. **21**, 3458 (2009).
[44] R. F. Egerton, Rep. Prog. Phys. **72**, 016502 (2009).
[45] S. J. Pennycook, M. F. Chisholm, A. R. Lupini, M. Varela, A. Y. Borisevich, M. P. Oxley, W. D. Luo, K. van Benthem, S.-H. Oh, D. L. Sales, S. I. Molina, J. García-Barriocanal, C. Leon, J. Santamaría, S. N. Rashkeev, and S. T. Pantelides, Philos. Trans. R. Soc. A **367**, 3709 (2009).

[46] P. Blaha, K. Schwarz, G. K. H. Madsen, D. Kvasnicka, and J. Luitz, *WIEN2k: An Augmented Plane Wave + Local Orbitals Program for Calculating Crystal Properties* (Karlheinz Schwarz, Techn. Universität Wien, Austria, 2001).
[47] H. T. Jeng, G. Y. Guo, and D. J. Huang, Phys. Rev. Lett. **93**, 156403 (2004).
[48] N. M. Caffrey, D. Fritsch, T. Archer, S. Sanvito, and C. Ederer, Phys. Rev. B **87**, 024419 (2013).
[49] H. T. Jeng and G. Y. Guo, Phys. Rev. B **65**, 094429 (2002).
[50] K. Dileep, B. Loukya, N. Pachauri, A. Gupta, and R. Datta, J. Appl. Phys. **116**, 103505 (2014).
[51] I. Dzyaloshinskii, J. Phys. Chem. Solids **4**, 241 (1958).
[52] T. Moriya, Phys. Rev. **120**, 91 (1960).
[53] Y. S. Hou, H. J. Xiang, and X. G. Gong, New J. Phys. **18**, 043007 (2016).
[54] P. Liu, S. Khmelevskyi, B. Kim, M. Marsman, D. Li, X.-Q. Chen, D. D. Sarma, G. Kresse, and C. Franchini, Phys. Rev. B **92**, 054428 (2015).
[55] M. Bode, M. Heide, K. V. Bergmann, P. Ferriani, S. Heinze, G. Bihlmayer, A. Kubetzka, O. Pietzsch, S. Blugel, and R. Wiesendanger, Nature **447**, 190 (2007).
[56] C. Weingart, N. Spaldin, and E. Bousquet, Phys. Rev. B **86**, 094413 (2012).
[57] P. W. Ma and S. L. Dudarev, Phys. Rev. B **91**, 054420 (2015).
[58] H. J. Xiang, E. J. Kan, Su-Huai Wei, M. H. Whangbo, and X. G. Gong, Phys. Rev. B **84**, 224429 (2011).
[59] B. H. Kim and B. I. Min, New J. Phys. **13**, 073034 (2011).
[60] A. Crepieux and C. Lacroix, J. Magn. Magn. Mater. **182**, 341 (1998).